RESEARCH ARTICLE

TECHNIQUES AND RESOURCES

Automated multidimensional image analysis reveals a role for Abl in embryonic wound repair

Teresa Zulueta-Coarasa[1], Masako Tamada[2], Eun J. Lee[1] and Rodrigo Fernandez-Gonzalez[1,3,4,*]

ABSTRACT

The embryonic epidermis displays a remarkable ability to repair wounds rapidly. Embryonic wound repair is driven by the evolutionary conserved redistribution of cytoskeletal and junctional proteins around the wound. *Drosophila* has emerged as a model to screen for factors implicated in wound closure. However, genetic screens have been limited by the use of manual analysis methods. We introduce MEDUSA, a novel image-analysis tool for the automated quantification of multicellular and molecular dynamics from time-lapse confocal microscopy data. We validate MEDUSA by quantifying wound closure in *Drosophila* embryos, and we show that the results of our automated analysis are comparable to analysis by manual delineation and tracking of the wounds, while significantly reducing the processing time. We demonstrate that MEDUSA can also be applied to the investigation of cellular behaviors in three and four dimensions. Using MEDUSA, we find that the conserved nonreceptor tyrosine kinase Abelson (Abl) contributes to rapid embryonic wound closure. We demonstrate that Abl plays a role in the organization of filamentous actin and the redistribution of the junctional protein β-catenin at the wound margin during embryonic wound repair. Finally, we discuss different models for the role of Abl in the regulation of actin architecture and adhesion dynamics at the wound margin.

KEY WORDS: Epithelial morphogenesis, Junctional dynamics, Mechanical forces, Quantitative image analysis, Segmentation algorithms, Wound healing, *Drosophila*

INTRODUCTION

Epithelial tissues display an ability to repair wounds. This ability is remarkable in embryos, in which epidermal wounds heal rapidly, with little inflammation and no scarring (Rowlatt, 1979). The rapid embryonic response to wounds is conserved across species, from fruit flies to humans (Longaker et al., 1990; McCluskey and Martin, 1995; Rowlatt, 1979; Whitby and Ferguson, 1991). Therefore, understanding the molecular mechanisms of embryonic wound repair might help to develop strategies to accelerate wound healing in adults (Degen and Gourdie, 2012; Sonnemann and Bement, 2011).

Embryonic wound repair is driven by the reorganization of cytoskeletal and junctional proteins. Actin and the motor protein non-muscle myosin II localize at the wound margin in the cells adjacent to the wound, forming a supracellular cable around the wound (Martin and Lewis, 1992). This actomyosin cable contracts,

serving as a 'purse string' that contributes to wound closure (Fernandez-Gonzalez and Zallen, 2013). The junctional molecules E-cadherin and α-catenin are depleted from the interfaces between wounded and adjacent cells, and accumulate at tricellular vertices at the wound margin (Abreu-Blanco et al., 2012; Brock et al., 1996; Wood et al., 2002). The redistribution of junctional proteins during wound repair is thought to provide discrete anchor points for the assembly of a contractile purse string around the wound. However, the mechanisms that regulate the redistribution of cytoskeletal and junctional proteins during embryonic wound healing are not well understood.

Drosophila has emerged as a model to investigate embryonic wound repair (Abreu-Blanco et al., 2012, 2011; Fernandez-Gonzalez and Zallen, 2013; Kiehart et al., 2000; Pickering et al., 2013; Wood et al., 2002). The genetic tractability of *Drosophila* allows the use of genetic screening to identify novel molecules implicated in embryonic wound healing (Campos et al., 2010; Juarez et al., 2011). However, the throughput of genetic screens has been limited by the use of manual, time-consuming analyses. Furthermore, wound healing screens have included limited dynamic information, thus hindering the detection of phenotypes that do not inhibit wound repair but do affect its dynamics.

We introduce a novel image-analysis tool for the automated quantification of three-dimensional (3D) cell behavior and wound-closure dynamics from confocal microscopy data. We demonstrate that our tool produces results similar to those obtained by manual and semi-automated methods, while reducing the analysis time. We show that our algorithm is applicable to the study of cell behavior in four dimensions. We use our tool to identify and quantify a wound-closure phenotype in mutants for the nonreceptor tyrosine kinase Abl, and we show that Abl contributes to the organization of actin and the redistribution of junctional proteins during embryonic wound repair. We propose that the use of automated image analysis in combination with time-lapse confocal microscopy will enable rapid screening of cellular and molecular dynamics during embryonic wound closure.

RESULTS

MEDUSA, an algorithm for automated image segmentation in confocal microscopy

The analysis of fluorescence microscopy images requires identification and delineation of objects (molecules, cells, tissues) for further quantitation. We developed an algorithm for multidimensional image delineation using snakes (termed 'MEDUSA'), which allows automated delineation of cellular and multicellular structures from fluorescence microscopy images. MEDUSA is based on snakes, an active contour method in which a polygon searches for its lowest energy configuration as it moves on an image (Fig. 1A). We defined the energy of the polygon (Eqn 1) to be lower when the polygon was short and smooth (Eqn 2) on regions of the image where fluorescence changed abruptly, such as object boundaries (Eqn 3). The result of the

[1]Institute of Biomaterials and Biomedical Engineering, University of Toronto, Toronto, ON, Canada M5S 3G9. [2]Developmental Biology Program, Sloan-Kettering Institute, New York, NY 10065, USA. [3]Department of Cell and Systems Biology, University of Toronto, Toronto, ON, Canada M5S 3G5. [4]Developmental and Stem Cell Biology Program, The Hospital for Sick Children, Toronto, ON, Canada M5G 1X8.

*Author for correspondence (rodrigo.fernandez.gonzalez@utoronto.ca)
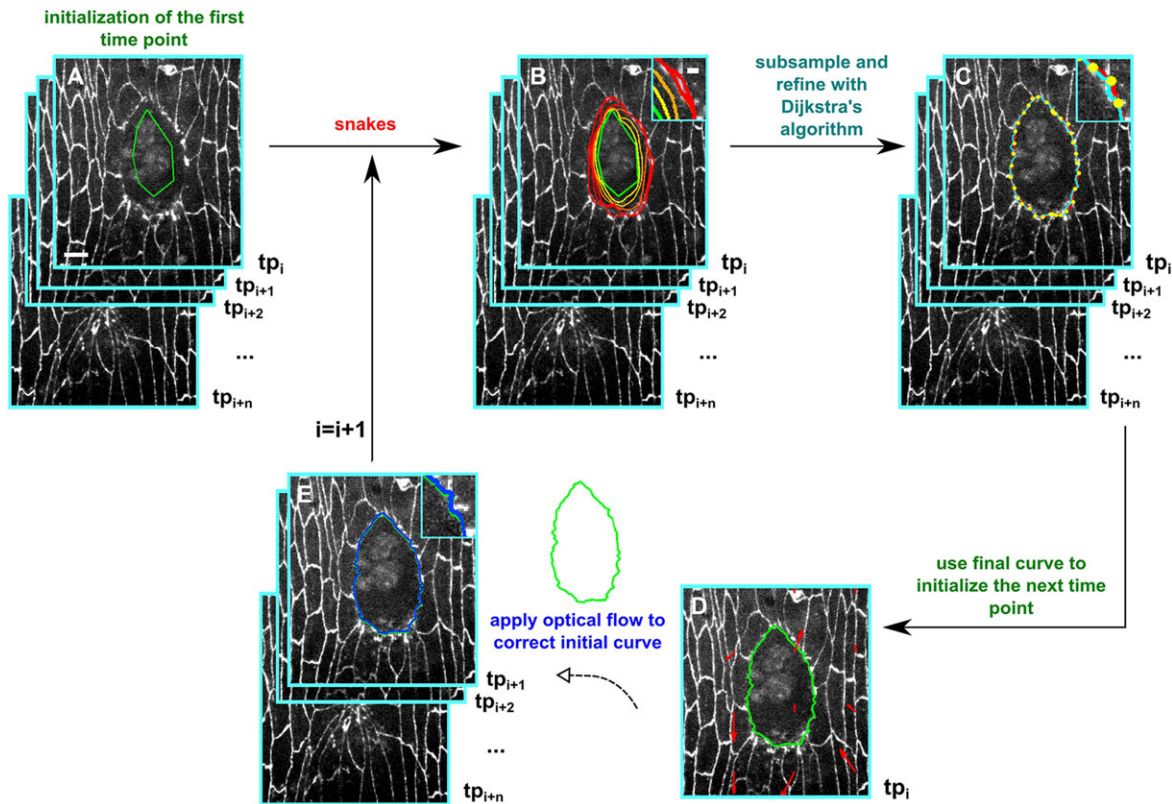
DEVELOPMENT

Fig. 1. MEDUSA, a tool for automated wound delineation in confocal microscopy images. (A) A user-drawn contour (green) initializes a snake in one of the movie time points. (B) The snakes algorithm runs an iterative energy minimization process. Initial contour (green), final contour (red) and intermediate steps (yellow-orange). (C) The result of snakes (red) is subsampled, generating a set of points (yellow dots). Dijkstra's algorithm is applied to find the brightest path between these points (cyan). (D,E) The final contour in tp_i (green) is transferred to tp_{i+1} after shifting by the optical-flow-indicated displacement (blue). Red arrows indicate the direction and magnitude of the optical flow. Scale bar: 5 µm; in inset: 1 µm.

energy-minimization process was a smooth polygon that outlined the object boundaries (Fig. 1B). To refine the results for non-smooth objects, such as wounds, we added a second, automated, step in which points were selected along the polygon, and the brightest path between these points was identified using Dijkstra's algorithm for optimal path search (Fig. 1C). The resulting polygon was projected on the next image in the sequence after shifting the polygon coordinates by the values that maximized the similarity between the two images, measured by cross-correlation (Fig. 1D,E). The iteration of energy minimization, optimal path search and polygon projection allowed automated delineation in the third dimension (time or z).

Automated quantification of wound-closure dynamics: validation of the algorithm

To validate MEDUSA, we delineated wounds in *Drosophila* embryos expressing the junctional marker β-catenin:GFP. Experiments were conducted at stage 14 of embryonic development, in which wound closure consists of a fast phase, followed by a slow phase (Abreu-Blanco et al., 2012; Fernandez-Gonzalez and Zallen, 2013). Embryos were wounded by pulsing a high-power ultraviolet laser along a 14 µm line on the epidermis of the animal, creating wounds with an area of 1078±41 µm². We compared three methods to quantify wound closure: manual tracing, a semi-automated method known as the LiveWire (Fernandez-Gonzalez and Zallen, 2013) and MEDUSA (Fig. 2A,B and supplementary material Fig. S2A,B). For each method, we quantified the dynamics of wound area, perimeter and fluorescence at the wound margin.

Wound area and fluorescence measurements were not significantly different for the three methods (Fig. 2C,E and supplementary material Fig. S2C,E). The wound-closure rates during the fast phase were 44.3±4.5, 45.1±4.7 and 45.2±4.6 µm²/min for manual tracing, LiveWire and MEDUSA, respectively (Fig. 2C and supplementary material Fig. S2C). Manual and MEDUSA-automated wound area measurements deviated during the final stages of wound closure (Fig. 2C‴, arrowhead, average difference was 7.8±1.6 µm²). This difference was due to the small wound size and the accumulation of debris towards the end of closure, which made it difficult to assess the position of the wound outline visually. Consequently, manual delineation becomes subjective and can differ from automated methods.

The measurements of wound perimeter obtained using LiveWire and MEDUSA were not significantly different (supplementary material Fig. S2D-D‴), but they were significantly greater than the manual measurements (Fig. 2D-D‴, P=0.01). This difference was due to the generation of smoother contours consisting of significantly fewer points by manual tracing than by Dijkstra's algorithm, which is used by both LiveWire and MEDUSA. To confirm this, we applied a Gaussian filter (σ=2 µm) to smoothen the contours generated by MEDUSA (supplementary material Fig. S3A,B). The smoothened MEDUSA contours had perimeter measurements similar to those obtained manually (supplementary material Fig. S3C, P=0.84).

To quantify the benefit of using MEDUSA over other methods, we compared the average time necessary to delineate wounds in 13 movies (Table 1). MEDUSA reduced the required user time by 57.9%
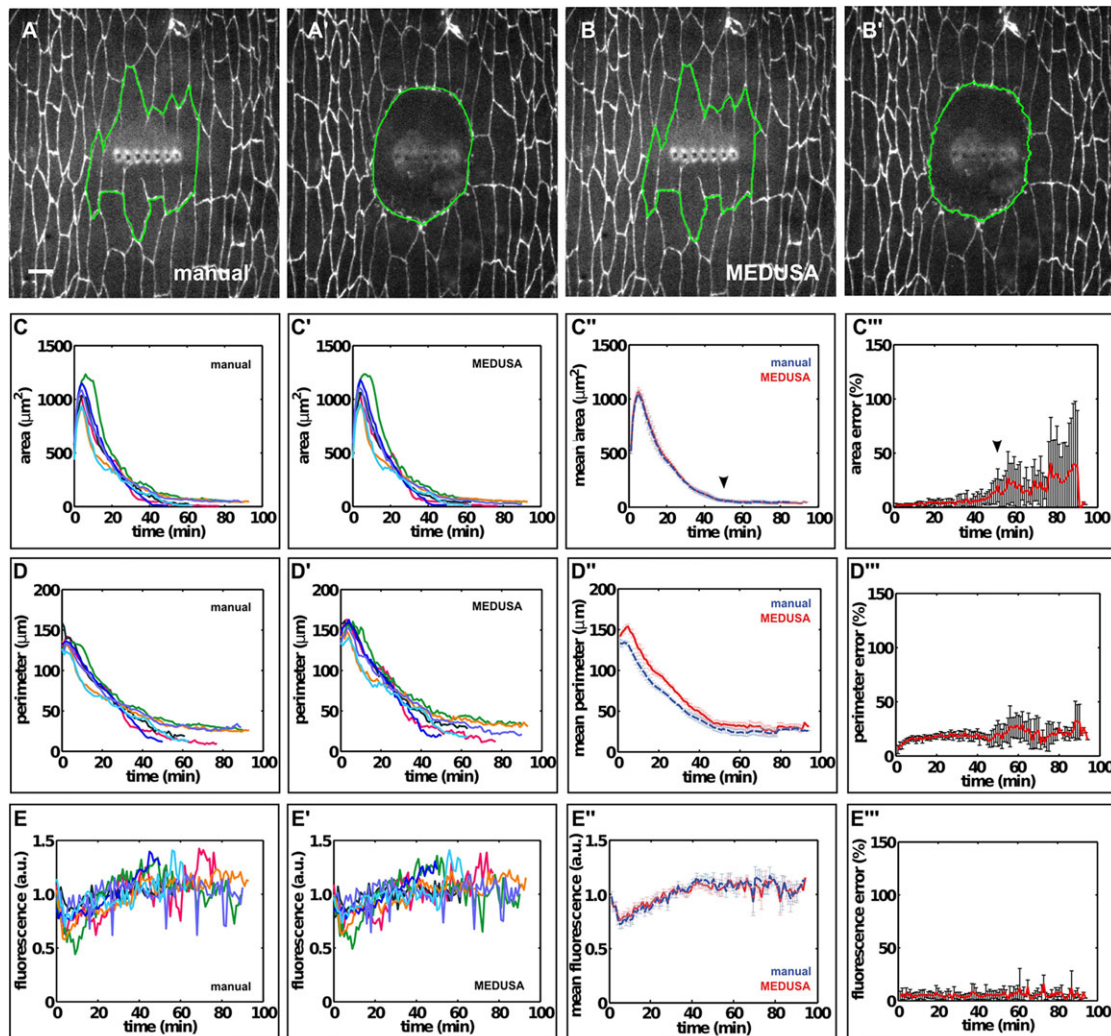
Fig. 2. Validation of automated wound delineation using MEDUSA. (A,B) Manual (A,A′) and automated (B,B′) wound delineation in embryos expressing β-catenin:GFP. (C-E) Wound area (C,C′), perimeter (D,D′) and fluorescence at the wound margin (E,E′) over time. Each line represents a different wound, and lines with the same color represent the same wound (*n*=7). (C″-E″) Average wound area (C″), perimeter (D″) and β-catenin:GFP fluorescence (E″) at the wound margin for manual (blue) and MEDUSA (red) delineation. (C‴-E‴) Average percentage difference (Eqn 5) in wound area (C‴), perimeter (D‴) and fluorescence (E‴) between MEDUSA and manual delineation. Time after wounding is indicated. Error bars, s.e.m. Scale bar: 5 μm.

when compared with LiveWire, and by 77.4% when compared with manual tracing of the wound outline. Most of the time required to delineate a wound using MEDUSA was unsupervised processing time, further demonstrating the advantages of automated wound delineation.

Four-dimensional cell tracking reveals morphological changes during embryonic wound closure

To demonstrate the generality of MEDUSA, we automatically quantified 3D cell morphology changes during *Drosophila* embryonic wound repair. We imaged wound closure during the elongation of the anterior-posterior axis in embryos expressing GFP:Rho1 to label the lateral surface of the cells. Wound closure during axis elongation is driven by the apical constriction of the wounded cells in combination with the assembly of an actomyosin purse string by the cells adjacent to the wound (Fernandez-Gonzalez and Zallen, 2013). At later stages of development, deformation of cells around the wound drives calcium influx through mechanically gated channels and promotes the assembly of the actomyosin purse string (Antunes et al., 2013). However, little is known about the cell

morphology changes that accompany wound repair during axis elongation. To investigate how the morphology of the apical domain of the cells changes during wound repair in early *Drosophila* embryos, we tracked the 3D shapes of 33 cells adjacent to wounds in three embryos. We delineated the apical domain of cells by initializing one snake per cell and by propagating the results of the segmentation to the adjacent *z*-planes, using the optical flow to adjust the position of the resulting contours (Fig. 3A-C; supplementary material Movie 1). We quantified morphological changes using a 3D shape factor. The shape factor was 1 for cylinders and 0 for flat sheets (Eqn 4). After wounding, a large majority of the cells around the wounds (24/33) expanded their apical domains (Fig. 3D-E, arrows in 3D′), resulting in a 17±2% decrease in the shape factor 3 min after wounding (Fig. 3F, $P=1.2\times10^{-7}$). This change was associated with a 22±3% increase in lateral surface area (Fig. 3G, 27/33 cells, $P=1.6\times10^{-7}$). The apical volume measured within 2.4 μm along the *z*-axis also increased by 26±4% (Fig. 3H, $P=1.5\times10^{-7}$). By contrast, during wound repair, the mean lateral surface area and volume of the apical domain decreased, returning to the levels measured before wounding

Table 1. Delineation time for different methods

Movie #	Number of time points	Manual (min)	LiveWire (min)	MEDUSA supervised (min)	MEDUSA unsupervised (min)
1	62	44.0	19.0	6.0	15.0
2	82	44.0	18.2	8.0	15.6
3	91	28.2	15.0	9.3	6.5
4	94	42.2	26.1	7.1	16.5
5	59	37.0	15.0	6.5	10.0
6	75	17.2	17.2	7.3	12.1
7	78	26.0	14.0	8.2	13.3
8	64	37.0	16.5	6.0	14.4
9	91	36.5	17.5	6.5	22.3
10	94	31.5	15.1	6.3	15.0
11	51	20.0	13.5	6.2	13.2
12	91	32.0	16.5	9.0	18.1
13	64	18.2	18.2	7.3	9.1
Average		31.8 (±2.6)	17.1 (±0.9)	7.2 (±0.3)	13.9 (±1.1)
Total	996				

Time required to delineate 13 movies using manual tracing, the LiveWire algorithm and MEDUSA (both supervised user time and unsupervised run time in which the algorithm runs without requiring user interaction).

(Fig. 3F,G). The rapid expansion of the lateral surface of the cells adjacent to the wound preceded the assembly and contraction of the actomyosin networks that drive wound closure (Fernandez-Gonzalez and Zallen, 2013), suggesting that the initial apical deformation of the cells around the wound might provide signals that trigger wound repair during axis elongation. Our data also suggest that an initial increase of the apical cell volume after wounding facilitates the subsequent apical expansion of the cells adjacent to the wound to cover the damaged region (Fernandez-Gonzalez and Zallen, 2013). Together, our results demonstrate that MEDUSA can be applied to the investigation of 3D cell morphology during epithelial morphogenesis.

Abelson kinase contributes to rapid wound repair in *Drosophila* embryos

Molecules that localize at the interface between wounded and adjacent cells are likely to play a role in wound repair (Abreu-Blanco et al., 2012; Bement et al., 1993; Martin and Lewis, 1992; Wood et al., 2002). To identify regulators of embryonic wound repair, we are currently using MEDUSA to screen for molecules that localize at the wound margin in *Drosophila* embryos. To this end, we wound embryos expressing a GFP-fused molecule and myosin:mCherry, and acquire time-lapse sequences of wound repair. Using MEDUSA, we can automatically detect candidate molecules that accumulate around wounds, and score these molecules based on their degree of enrichment with respect to myosin. We found that Abl accumulated at the wound margin (Fig. 4A-C and supplementary material Movie 2). Abl was enriched by 2.4±0.1-fold at the purse string (n=3, Fig. 4D). The enrichment of Abl at the wound margin was lower than the enrichment of myosin (3.1±0.2-fold, P=0.05, Fig. 4D), demonstrating that our approach can detect subtle localization patterns. Our data suggest that Abl plays a role in embryonic wound closure.

To assess whether Abl participates in embryonic wound repair in *Drosophila*, we used MEDUSA to compare the dynamics of wound closure in wild-type embryos and in *abl* mutants. Wounds were significantly larger in the wild type (WT) than in *abl* mutants (maximum wound area was 1078±41 μm^2 in WT and 881±79 μm^2 in *abl*, P=0.04, Fig. 5A-C). These data suggest that epidermal cells sustain more tension in WT than in *abl* mutants. Consistent with

this, *abl* mutants displayed a 19.1% reduction in apical cell area (P=1.8×10^{-7}) and a 17.1% reduction in cell elongation along the dorsal-ventral axis (P=3.9×10^{-5}) (supplementary material Fig. S4). Notably, the rate of wound closure during the fast phase was greater in wild-type embryos (45.2±4.6 μm^2/min) than in *abl* mutants (28.5±4.7 μm^2/min, Fig. 5D, P=0.02). Wild-type embryos responded to wounds more homogeneously than mutants, as quantified by the standard deviation of the wound area across embryos averaged over time, which was smaller for wild-type embryos (52±5 μm^2) than for *abl* mutants (121±5 μm^2) (Fig. 5C,C′, P=3.9×10^{-19}). These results indicate that Abl contributes to rapid embryonic wound repair in *Drosophila*.

β-catenin is dynamically regulated during embryonic wound repair in *Drosophila*

Abl regulates the localization of the junctional protein β-catenin in *Drosophila* embryos (Grevengoed et al., 2001; Tamada et al., 2012). In wound closure, the junctional molecules E-cadherin and α-catenin are depleted from the wound perimeter and accumulate at tricellular vertices between wounded and adjacent cells (Abreu-Blanco et al., 2012; Brock et al., 1996; Wood et al., 2002). We used MEDUSA to determine whether β-catenin was also redistributed during wound closure. We delineated wounds in embryos expressing β-catenin:GFP and quantified β-catenin fluorescence in single edges at the wound margin. β-catenin fluorescence at interfaces between wounded and adjacent cells decreased by 21.7±3.2% within 12 min of wounding (Fig. 6A,B, P=5.5×10^{-7}). By contrast, β-catenin:GFP fluorescence increased by 22.1±5.0% at tricellular vertices around the wound (Fig. 6A,B, P=4.1×10^{-4}). Therefore, β-catenin is dynamically regulated at the wound margin during tissue repair.

The accumulation of junctional proteins in tricellular vertices at the wound margin could be a prerequisite for the contraction of an actomyosin purse string anchored at those points. Alternatively, the accumulation of junctional proteins in vertices could be a response to the mechanical forces that purse string contraction generates on the points of contact between cells around the wound. We quantified the relative timing of β-catenin redistribution at the wound margin with respect to purse string contraction. Loss of β-catenin from the wound margin began 1 min after wounding, while the wound was expanding, and finished within 4 min (Fig. 6C). By contrast, β-catenin accumulation in tricellular vertices did not begin until the onset of wound closure, 4 min after wounding, and continued while the purse string contracted (Fig. 6C). These data raise the possibility that accumulation of β-catenin in tricellular vertices around the wound is a consequence of, rather than a prerequisite for, the assembly of a contractile actomyosin purse string.

Abl is necessary for β-catenin dynamics during embryonic wound repair

Abl can disrupt and promote cell adhesion in *Drosophila* embryos. During axis elongation, Abl directs junctional disassembly by increasing β-catenin turnover and displacing β-catenin from cell junctions (Tamada et al., 2012). Conversely, in the late embryonic epidermis, Abl is necessary for adherens junction maintenance and β-catenin localization to cell junctions (Grevengoed et al., 2001). To determine whether Abl regulates β-catenin dynamics at the wound margin, we used MEDUSA to quantify changes in β-catenin:GFP fluorescence during wound closure in *abl* mutants. β-catenin:GFP fluorescence decreased at the interface between wounded and adjacent cells in *abl* mutants (Fig. 7A,B). The depletion of β-catenin from the wound margin in *abl* mutants was slower than in WT (Fig. 7C, P=0.04), but the degree of depletion
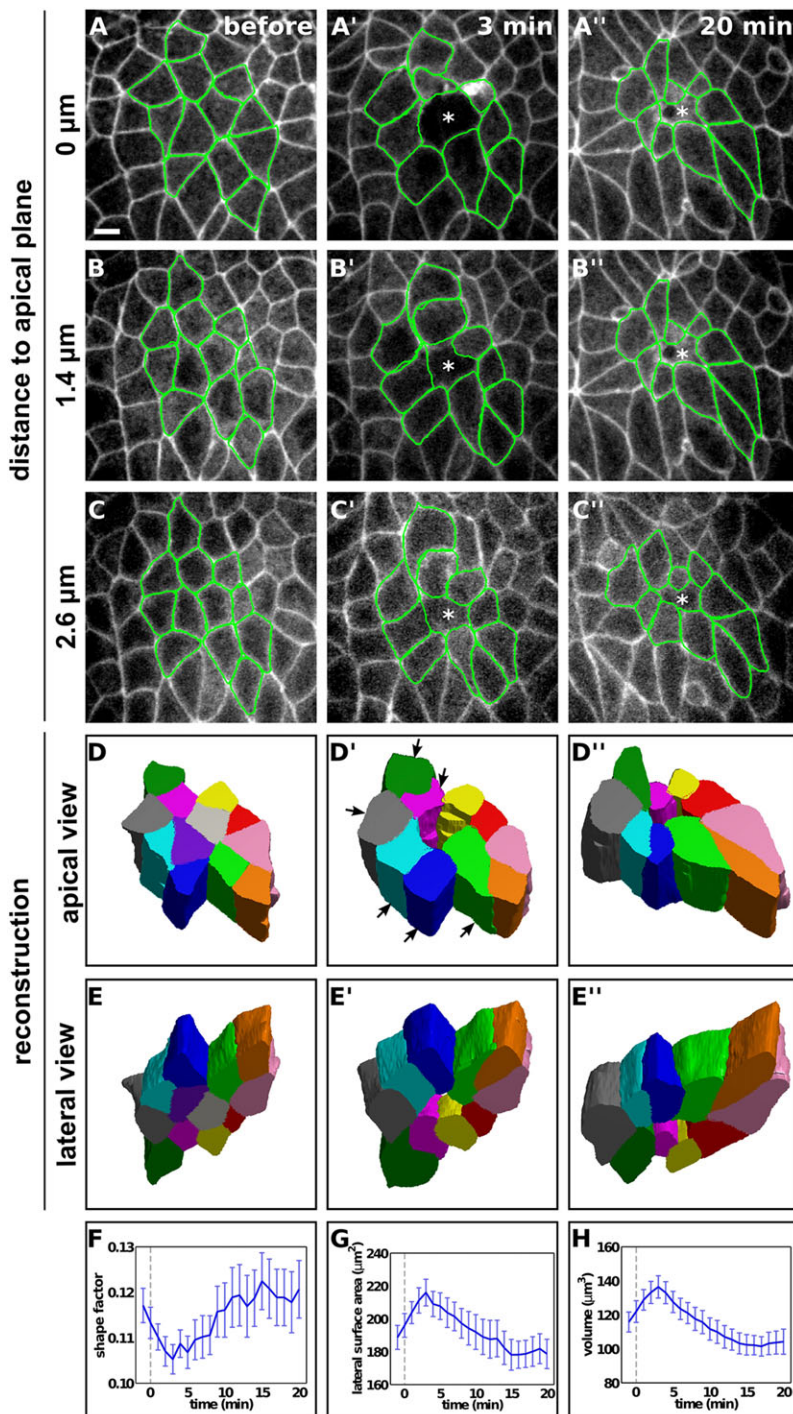
Fig. 3. Automated reconstruction of cells around a wound using MEDUSA. (A-C) Automated delineation of cells surrounding a wound in three different time points (columns) and three z-planes (rows, distance indicated from the most apical plane segmented). Images are from a stage 7 embryo expressing GFP:Rho1. Asterisks show the position of the wound. Scale bar: 5 μm. Anterior left, dorsal up. (A-A″) Time after wounding is indicated. (D,E) The results of MEDUSA in 13 z-planes per stack were reconstructed in 3D from apical (D) and lateral (E) perspectives. Arrows in D′ indicate cells that expand upon wounding. (F-H) Shape factor (F), lateral surface area (G) and apical volume (H) of cells adjacent to the wound (n=33 cells). Gray dashed lines show the first time point after wounding. Error bars, s.e.m.

12 min after wounding in *abl* mutants (20.6±3.2%, Fig. 7A,B) was not significantly different from WT. These data suggest that Abl regulates the dynamics of β-catenin depletion from the wound margin during embryonic wound closure.

We next investigated β-catenin dynamics in tricellular vertices around the wound in *abl* mutants. β-catenin:GFP fluorescence in tricellular vertices did not increase significantly in *abl* mutants (5.6±6.2%, Fig. 7A,B). As a consequence, β-catenin:GFP accumulation in tricellular vertices 15 min after wounding was significantly lower in *abl* mutants than in WT (Fig. 7D and supplementary material Movie 3, $P=8.3\times10^{-3}$). In *abl* mutants, there was no correlation between purse string contraction and β-catenin accumulation in

tricellular vertices around the wound (Fig. 7C). Together, these data suggest that Abl might be necessary for efficient purse string contraction and β-catenin localization to tricellular vertices during embryonic wound closure.

Abl is necessary for actin organization and filopodial dynamics during wound repair

Myosin-dependent contractility can be regulated by actin organization (Reymann et al., 2012). Abl controls actin organization by restricting the localization of Enabled (Fox and Peifer, 2007; Grevengoed et al., 2003, 2001), an actin regulator that promotes formation of long, unbranched filaments (Bear et al., 2002). To determine whether Abl
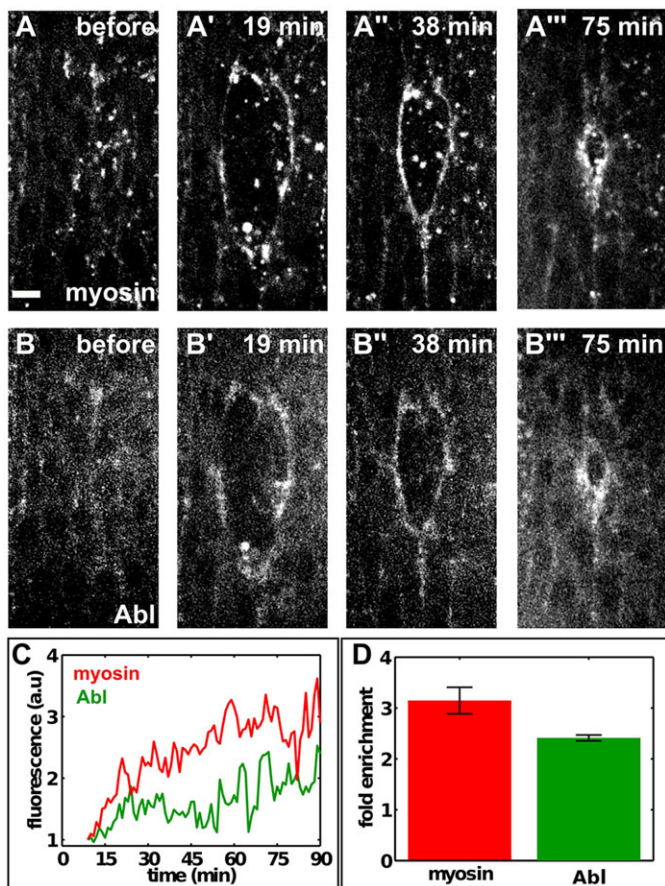
Fig. 4. Abl accumulates around epidermal wounds. (A,B) Epidermal cells expressing myosin:mCherry (A-A‴) and Abl:GFP (B-B‴) in a stage 14 embryo. Scale bar: 5 μm. Anterior left, dorsal up. (C) Quantification of fluorescence intensity at the wound margin for Abl:GFP (green) and myosin:mCherry (red) for the wound shown in A,B. (A-C) Time after wounding is indicated. (D) Maximum fold enrichment of myosin:mCherry and Abl:GFP (n=3). Error bars, s.e.m.

controls actin organization at the purse string during embryonic wound repair, we used MEDUSA to quantify actin fluorescence at the wound margin in embryos expressing GFP:moesin (Kiehart et al., 2000). Actin fluorescence was measured in a 0.6 μm-wide mask overlaid on the purse string. This mask was thinner than the purse string to exclude actin-based protrusions from the analysis. Actin fluorescence at the purse string was heterogeneous in WT, with regions of high and low intensity (Fig. 8A, arrows). This is consistent with an asymmetric distribution of actin at the purse string, similar to that observed in the actomyosin ring that drives cytokinesis in the nematode *Caenorhabditis elegans* (Maddox et al., 2007). By contrast, in *abl* mutants, distribution of actin at the purse string was homogeneous (Fig. 8B). We divided the purse string into quadrants and quantified actin heterogeneity as the standard deviation of actin fluorescence in the quadrants. On average, actin heterogeneity at the purse string was 68.0±14.7% greater in WT than in *abl* during the first 12 min after purse string assembly (8-20 min after wounding, Fig. 8C, $P=5.2\times10^{-4}$). These data indicate that actin organization at the purse string is disrupted in *abl* mutants and suggest the presence of a defect in the mechanical properties of the purse string in *abl* mutants.

Loss of *abl* leads to increased protrusive activity, both in cultured cells and in embryos (Gates et al., 2007; Grevengoed et al., 2003). To establish whether protrusive activity is affected during wound repair in *abl* mutants, we extended MEDUSA to quantify cell protrusions. We measured the fraction of bright pixels within a narrow ring (~2.5 μm wide) immediately internal to the wound margin in embryos expressing GFP:moesin (supplementary material Fig. S5). Protrusive activity was 30.7±3.7% higher in *abl* mutants than in wild-type embryos during the first 12 min after purse string assembly (8-20 min after wounding, supplementary material Fig. S5, $P=5.2\times10^{-4}$), further indicating that actin dynamics at the wound margin are abnormal in *abl* mutants. Together, our data suggest that Abl regulates actin organization and junctional dynamics at the wound margin to promote rapid wound repair.

DISCUSSION

Here, we introduce MEDUSA, a novel tool for the automated delineation, tracking and quantitative analysis of epidermal wounds from time-lapse sequences. MEDUSA uses snakes, an active contour algorithm, in which a curve evolves on an image to minimize its energy (Kass et al., 1988). We define an energy function that is lowest for short, smooth curves on areas of the image where the pixel values change rapidly. Thus, energy minimization attracts the curve towards the wound margin. The outline of the resulting curve is refined using Dijkstra's algorithm (Dijkstra, 1959) between discrete points along the curve. The final curve is projected onto the adjacent time points after adjusting its position using the optical flow (Raffel et al., 1998), and the process is iterated. We demonstrate the use of MEDUSA by identifying a wound-closure phenotype in mutants for Abl, which regulates actin organization and junctional dynamics (Zandy and Pendergast, 2008).

MEDUSA uses active contour methods – snakes – to delineate the wound margin automatically. One of the advantages of active contours is that the morphology of the object to be delineated can be used to bias the algorithm (Kass et al., 1988). Other segmentation methods, such as the watershed (Beucher, 1992), only consider changes in signal intensity at the object boundaries, and fail to delineate objects that do not have continuous edges. Methods based on active contours have limitations when delineating objects with long, narrow protrusions or sharp corners, as these configurations are not favored during energy minimization. Reducing the weight of the energy term that promotes smooth boundaries can alleviate these limitations. Using MEDUSA, we delineated cells and wounds labeled with continuous markers, such as GFP:Rho1 or myosin: mCherry, by favoring image regions where pixel intensities changed substantially. We also used MEDUSA to delineate wounds labeled with patchy markers, such as β-catenin:GFP, by taking advantage of the morphological properties of the wound and enforcing smooth, convex contours. Active contours are computationally expensive as they require the solution of partial differential equations to minimize their energy (Kass et al., 1988). However, MEDUSA automatically projects the results obtained from one image onto the next, thus facilitating the energy minimization process, and the algorithm can run unsupervised. The user only needs to set the parameters that determine the relative weight of the morphological and intensity factors during energy minimization (Kass et al., 1988). We are currently developing machine learning methods for the automated selection of parameter values based on training sets obtained using different fluorescent markers, image resolutions and stages of animal development (Duda et al., 2000).

We are using MEDUSA to identify molecules that regulate embryonic wound repair. Several studies have screened for genes that affect wound closure in *Drosophila* (Campos et al., 2010; Juarez et al., 2011; Lesch et al., 2010). These efforts revealed novel molecules implicated in wound repair, but did not cover the entire
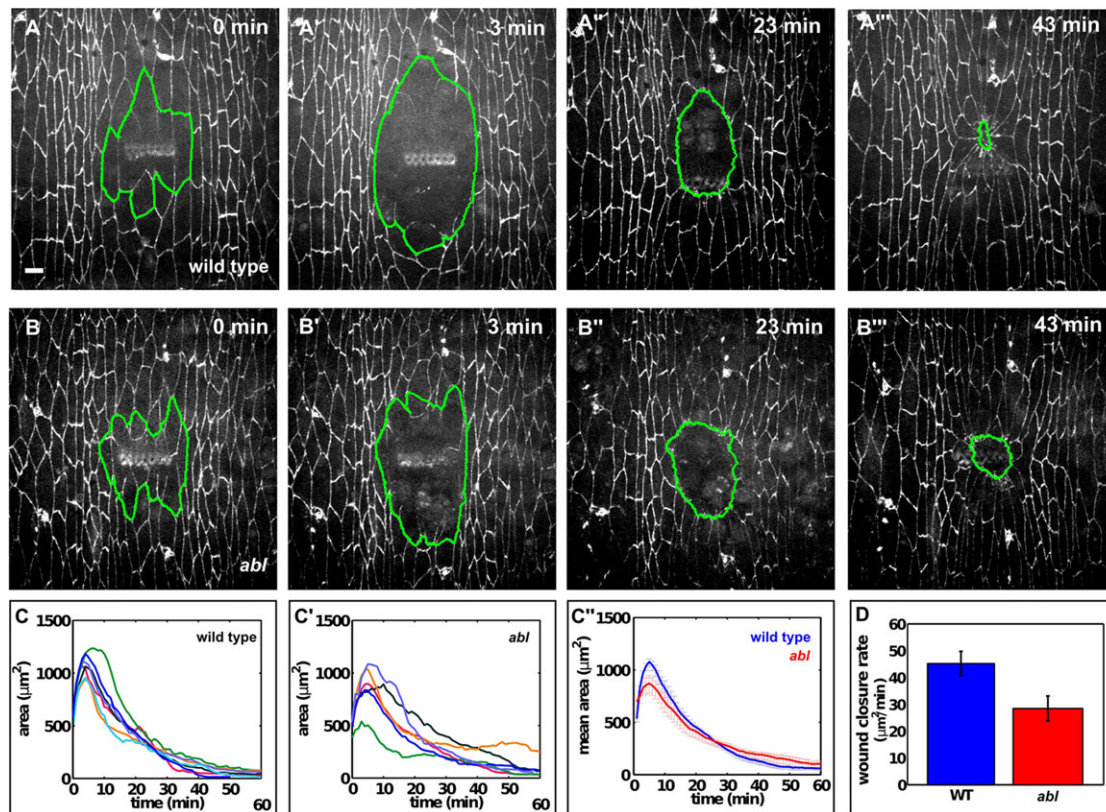
DEVELOPMENT

Fig. 5. Faster wound closure in wild-type embryos than in *abl* mutants. (A,B) Wound closure in wild-type (A-A‴) and *abl* mutant embryos (B-B‴) expressing β-catenin:GFP. Time after wounding is indicated. Scale bar: 5 μm. Anterior left, dorsal up. (C-C″) Wound area over time in wild-type embryos (C, *n*=7), *abl* mutants (C′, *n*=6) and average values (C″). (C,C′) Each color represents an individual wound. (D) Mean wound-closure rate during the fast phase of tissue repair. Error bars, s.e.m.

genome, as screening was manual and time consuming. Furthermore, previous attempts to screen for regulators of wound closure usually involved long 'incubation' periods after wounding, in which wound repair proceeded unmonitored. Therefore, these screens have identified factors strictly necessary for wound closure, but have failed to detect molecules that modulate the wound repair response. To overcome this limitation, image-based screening combined with automated image analysis can detect and quantitate phenotypes associated with wound-closure dynamics. The use of tools such as MEDUSA, in combination with automated microscopy, will greatly facilitate this form of screening.

Using MEDUSA, we quantified the dynamics of adherens junctions around epidermal wounds. β-catenin was rapidly depleted from the wound margin and accumulated at tricellular vertices between wounded and adjacent cells. This distribution is similar to that of other junctional proteins, such as E-cadherin (Brock et al., 1996; Abreu-Blanco, 2012) and α-catenin (Wood et al., 2002). The depletion of β-catenin from the wound margin might facilitate disassembly of the junctions between wounded and adjacent cells. It has been proposed that the accumulation of junctional proteins in tricellular vertices at the wound margin is necessary for actomyosin contractility around the wound by providing anchor points for the
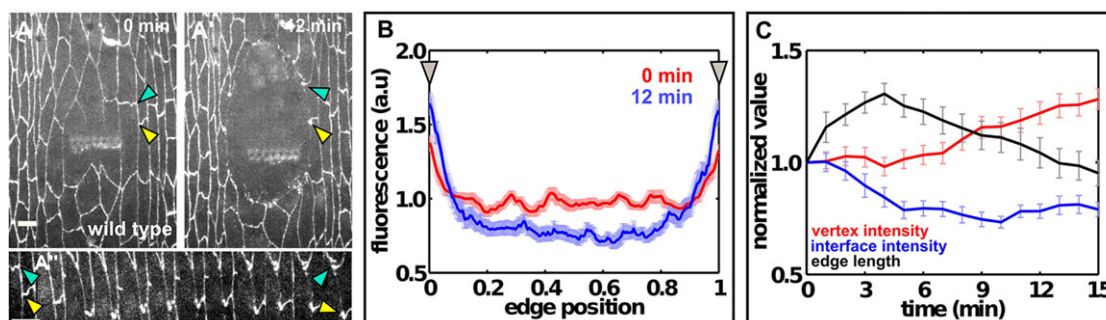

Fig. 6. β-catenin is dynamically regulated in embryonic wound repair. (A,A′) Cells expressing β-catenin:GFP in a wild-type embryo. Arrowheads indicate the position of an edge that will be at the wound margin. Time after wounding is indicated. Scale bar: 5 μm. Anterior left, dorsal up. (A″) Kymograph showing the redistribution of β-catenin:GFP at the edge indicated in (A). Scale bar: 1 min. (B) Mean β-catenin:GFP fluorescence along cell edges at the wound margin in wild-type embryos immediately after wounding (red) and 12 min later (blue). Tricellular vertices are at the two ends of edges at the wound margin (arrowheads). Fluorescence values were normalized to the average fluorescence along each interface at *t*=0 min. (C) Relative edge length (black), vertex intensity (red) and interface intensity (blue) during the initial 15 min of wound repair. (B,C) Error bars, s.e.m.; *n*=35.
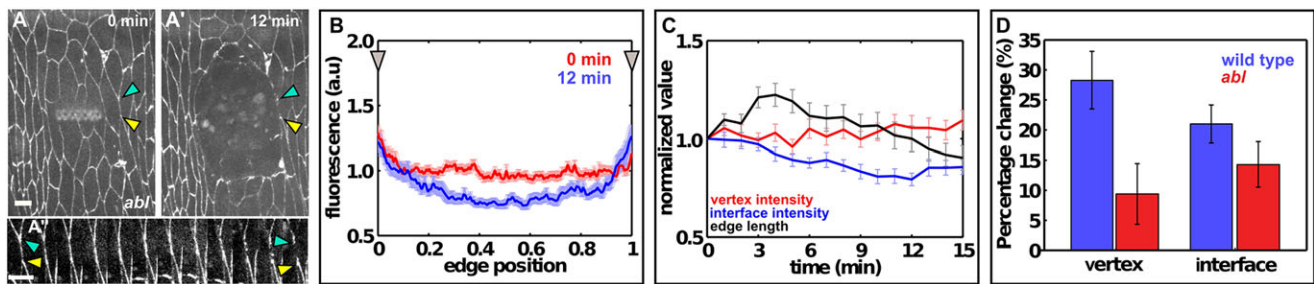
Fig. 7. β-catenin accumulation at tricellular vertices is defective in *abl* mutants. (A,A′) Cells expressing β-catenin:GFP in an *abl* mutant. Arrowheads indicate the position of an edge that will be at the wound margin. Time after wounding is indicated. Scale bar: 5 μm. Anterior left, dorsal up. (A″) Kymograph showing the redistribution of β-catenin:GFP at the edge indicated in A. Scale bar: 1 min. (B) Mean β-catenin:GFP fluorescence along cell edges at the wound margin in *abl* mutants immediately after wounding (red) and 12 min later (blue). Tricellular vertices are at the two ends of edges at the wound margin (arrowheads). Fluorescence values were normalized to the average fluorescence along each interface at *t*=0 min. (C) Relative edge length (black), vertex intensity (red) and interface intensity (blue) during the initial 15 min of wound repair. (D) Percentage change of β-catenin:GFP fluorescence 15 min after wounding in WT (blue) and *abl* mutants (red) in tricellular vertices (percentages indicate increase) and interfaces (percentages indicate decrease). (B-D) Error bars, s.e.m.; *n*=35.

purse string and hence facilitating the transmission of mechanical forces. However, we found that β-catenin accumulation in tricellular vertices around the wound occurred in parallel with purse string contraction, rather than preceding it. These results suggest that the accumulation of junctional proteins at discrete points on the wound margin might result from the tension generated by the actomyosin purse string. Future experiments modulating tension at the wound margin should reveal the role of mechanical forces on junctional dynamics during embryonic wound repair.

We found that Abl localizes around epidermal wounds and contributes to actin organization, adherens junction redistribution and rapid wound repair in *Drosophila*. During axis elongation, Abl can phosphorylate and promote the turnover of β-catenin, thus favoring junctional disassembly (Tamada et al., 2012). At later stages of embryonic development, Abl is necessary to maintain β-catenin at the adherens junctions between epidermal cells (Grevengoed et al., 2001). Depletion of β-catenin from the wound margin in *abl* mutants was slower than in WT, suggesting that Abl is necessary to remove β-catenin rapidly from the interface between wounded and adjacent cells. In *abl* mutants, the accumulation of β-catenin in tricellular vertices at the wound margin was defective. These data suggest that Abl plays a role in the depletion of β-catenin from the wound margin and its accumulation in discrete points around the wound.

Abl regulates actin organization (Baum and Perrimon, 2001; Koleske et al., 1998), and actin organization can modulate

actomyosin contractility (Bendix et al., 2008; Janson et al., 1991; Köhler et al., 2011). Therefore, Abl could facilitate efficient purse string contraction that generates mechanical tension on tricellular vertices around the wound, thus resulting in the growth of mechanosensitive cadherin-catenin complexes (Liu et al., 2010) (Fig. 9). Actin distribution at the wound margin was heterogeneous in wild-type embryos, with segments of high and low actin density, suggesting that purse string contraction occurs asymmetrically. The heterogeneous actin distribution around the wound could facilitate the contraction of different segments of the purse string, or increase the robustness of the process (Maddox et al., 2007). Actin organization at the purse string was disrupted in *abl* mutants, in which it was more homogeneous than in WT. A homogeneous actin distribution at the purse string could resist the contraction of individual segments, thus slowing down wound closure. Defective actin organization at the purse string in *abl* mutant embryos was accompanied by an increase in protrusive activity. Together, our data strongly suggest that Abl is actively involved in wound repair, where it regulates actin polymerization and organization at the wound margin, possibly by restricting the localization of Ena (Gates et al., 2007; Grevengoed et al., 2003). However, changes in actin organization can affect the viscoelastic properties of cells (Janmey, 1991; Moulding et al., 2012); therefore, loss of Abl could also affect the wound-healing response by increasing the resistance to deformation of the cells around the wound. Further experiments will determine the role of Abl in actomyosin contractility at the
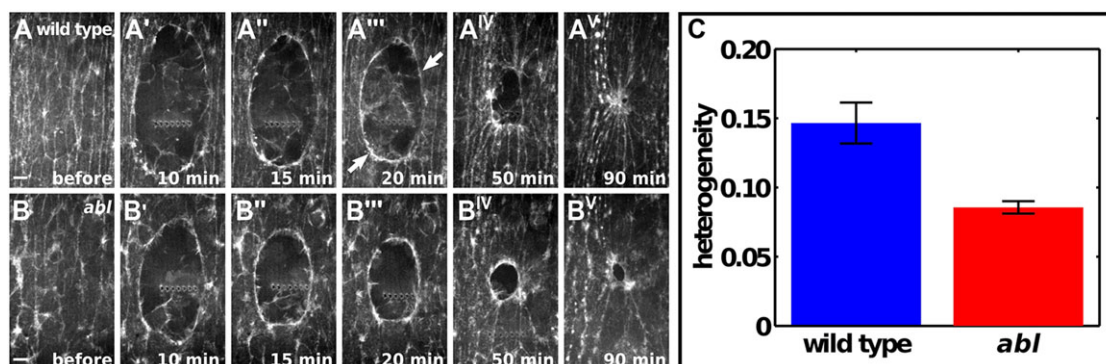

Fig. 8. Abl controls actin organization at the purse string in embryonic wound repair. (A,B) Wound closure in a wild-type embryo (A-A[V]) and an *abl* mutant (B-B[V]) expressing GFP:moesin. Arrows in A[III] indicate areas of high (left) and low (right) actin accumulation. Time after wounding is indicated. Scale bar: 5 μm. Anterior left, dorsal up. (C) Actin heterogeneity in the purse string for WT (blue, *n*=26 time points in two embryos) and *abl* (red, *n*=65 time points in five embryos). Error bars, s.e.m.
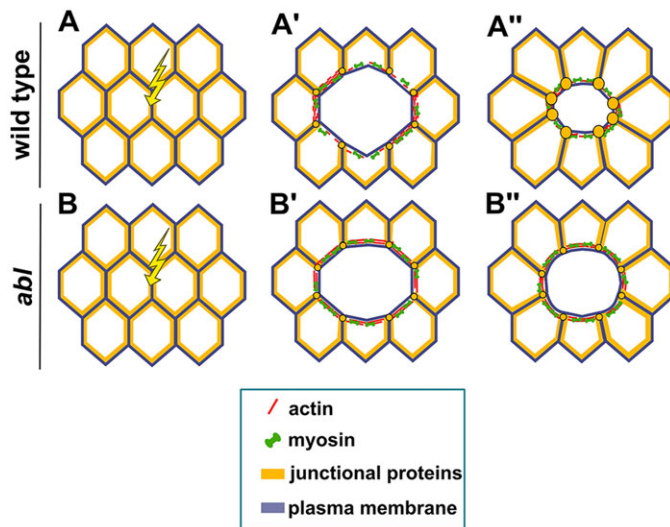
Fig. 9. A model for the role of Abl in embryonic wound repair. (A-A″) Upon wounding (yellow arrow, A,B), junctional proteins (orange) are depleted from the interface between wounded and adjacent cells (A′). An actomyosin purse string (red, green) of heterogeneous density is assembled around the wound (A′). Abl contributes to actin organization in the purse string, facilitating the generation of contractile forces on the contact points between cells adjacent to the wound. These forces might promote growth of mechanosensitive junctional complexes (A″). (B-B″) In *abl* mutants, junctional proteins are depleted from the wound margin (B), albeit more slowly than in WT. Actin organization at the purse string is defective (B′), disrupting the generation of mechanical forces at the points of contact between cells adjacent to the wound and the accumulation of junctional proteins at these points, and reducing the speed of wound closure (B″).

purse string and in cell and tissue mechanics. The use of MEDUSA has allowed us to identify a role for Abl in embryonic wound closure and to formulate novel hypotheses about the mechanisms by which Abl contributes to epithelial repair.

MATERIALS AND METHODS
Fly stocks
For live imaging we used β-catenin:GFP (McCartney et al., 2001), sqh: mCherry (Martin et al., 2010), Abl:GFP (Fox and Peifer, 2007) and GFP:Rho1 (Bloomington *Drosophila* Stock Center #9392). GFP:Rho1 embryos were the F2 progeny of *UAS-GFP:Rho1* males×*matαtub67;15* females (a gift from D. St Johnston, University of Cambridge, UK). β-catenin:GFP, sqh:mCherry and Abl:GFP were expressed from endogenous promoters. Germline clones were generated with the FLP-DFS system (Chou and Perrimon, 1996). *hs-FLP38*; *β-catenin:GFP*/+; *abl⁴ FRT2A/ovoD1 FRT2A* larvae were heat-shocked, and females were crossed to *β-catenin:GFP*/+; *abl⁴ FRT2A*/TM3, *twi-GAL4, UAS-GFP* males. For actin analysis, *hs-FLP38*; ; *abl⁴ FRT2A*, *GFP:moesin/ovoD1 FRT2A* larvae were heat-shocked, and females were crossed to *abl⁴ FRT2A*, *GFP:moesin*/TM3, *twi-Gal4:UAS-GFP* males. Homozygous mutant embryos were identified by the absence of fluorescence from *twi-Gal4:UAS-GFP*.

Time-lapse imaging
Embryos were dechorionated in 50% bleach for 2 min, washed and mounted in a 1:1 mix of halocarbon oil 27 and 700 (Sigma) between a cover glass and an oxygen-permeable membrane (YSI). Embryos were imaged using an Ultraview RS spinning disk confocal microscope (PerkinElmer) equipped with an Orca ER camera (Hamamatsu) and a 63× oil immersion lens (Zeiss, NA 1.4), or with a Revolution XD spinning disk confocal microscope equipped with an iXon Ultra 897 camera (Andor) and a 60× oil immersion lens (Olympus, NA 1.35). Every 15-60 s, 16-bit stacks were acquired. These stacks were projected for wound-closure analysis. Wounds were induced

using a pulsed Micropoint N_2 laser (Andor) tuned to 365 nm. For 3D analysis, stacks consisting of 13 slices 0.2 μm apart and acquired at 1 min intervals were delineated.

Automated delineation of wounds and cells
To automate the delineation of wounds and cells in multidimensional fluorescence microscopy images, we developed a novel method called MEDUSA, using Matlab (Mathworks) and the DIPImage toolbox (TU Delft, The Netherlands). MEDUSA is available for download at http://individual. utoronto.ca/quantmorph/software.html. MEDUSA is based on two image-analysis algorithms: snakes and Dijkstra's minimal path search.

Snakes
A snake is a dynamic contour that tries to minimize its energy by evolving on an image (Kass et al., 1988). Snakes can be parameterized using a variable $p \in [0,1]$, in which 0 indicates the beginning of the contour and 1 is the end, and a vector $\underline{s}(p) = [x(p), y(p)]$, in which x and y are functions that provide the coordinates along the contour. The energy of the snake, E_{snake}, can be defined as:

$$E_{snake} = \int_0^1 E_{\text{int}}(\underline{s}(p)) + E_{ext}(\underline{s}(p))dp, \tag{1}$$

in which E_{int} and E_{ext} are the internal and external energies of the snake, respectively. We defined the internal energy of the snake as:

$$E_{\text{int}} = \frac{1}{2}\left(\alpha(p)\left|\frac{ds}{dp}\right|^2 + \beta(p)\left|\frac{d^2s}{dp^2}\right|^2\right). \tag{2}$$

E_{int} depends on the first derivative of the curve, ds/dp, which is greater for longer curves; and on the second derivative of the curve, d^2s/dp^2, which is greater for irregular, convoluted curves. Minimization of E_{int} favors snakes that are short and smooth. α and β weight the relative importance of these terms. We experimentally chose the values for these parameters as $\alpha=3$, $\beta=5$ to delineate wounds, which had elliptical, smooth boundaries, and $\alpha=3$, $\beta=0.5$ to delineate epithelial cells, which had polygonal shapes that included protrusions and narrow regions.

We defined E_{ext} as:

$$E_{ext} = -||\nabla I(\underline{s})||^2, \tag{3}$$

in which $\nabla I(\underline{s})$ is the image gradient, a vector that points in the direction of maximum local intensity change, and the magnitude of which is proportional to the magnitude of that change. Minimization of E_{ext} attracts the snake towards areas of the image where intensity changes rapidly, such as the wound border or the boundaries of a cell expressing a fluorescent cell outline marker.

An internal pressure or balloon force was added to the external force to ensure that the snake was attracted towards the edge of the object to be delineated (Cohen and Cohen, 1993). The direction of the balloon force was given by $\underline{n}(p)$, the unit vector perpendicular to the snake at point $\underline{s}(p)$, and its amplitude was controlled by an external parameter, k. The balloon force is important when the initial snake is far from the object to delineate. A positive value for k inflates the snake, whereas a negative value will make it shrink. For wounds, we used k values from −0.6 to 0.6. For cells, which did not change their size substantially along the z-axis or in time, we used k values from −0.3 to 0.3.

We initialized a snake in one time point of the time-lapse sequence using a hand-drawn polygon (Fig. 1A) or the LiveWire-algorithm, a semi-automated segmentation method that provides an accurate initialization with minimal user interaction (Fernandez-Gonzalez and Zallen, 2011). The initial contour evolved under the forces described above until its area became stable, as determined by changes in snake area below a threshold of seven pixels (Fig. 1B). We used the Euler–Lagrange equation to achieve energy minimization (Bryant et al., 2003).

Refining snakes using Dijkstra
The contour resulting from the snakes algorithm does not always provide an accurate delineation of the object to be segmented (Fig. 1C, inset). To refine

the results from snakes, we took points nine pixels apart along the contour (Fig. 1C, yellow) and used Dijkstra's minimal path search algorithm (Dijkstra, 1959) to find the brightest path connecting consecutive points. To this end, we built a weighted graph in which each pixel was represented by a node, and nodes were connected if the corresponding pixels were at most $\sqrt{2}$ pixels apart (Fernandez-Gonzalez and Zallen, 2011). Connections between nodes were bidirectional and weighted by the inverted pixel value of the destination node, such that moving towards bright pixels was cheaper than moving towards dark pixels. Dijkstra's algorithm was used to find the minimal cost path between nodes in the graph that corresponded to pairs of points along the snake (Fig. 1C).

Projecting snakes onto neighboring time points
Active contours have been used to delineate multicellular structures in static images of epithelial tissues (Fernandez-Gonzalez et al., 2004; Hutson et al., 2003). To extend our analysis to time (and more generally, to three or four dimensions), the contour resulting from snakes and Dijkstra's algorithm in time point i of an image sequence was used to initialize the algorithm in the previous and subsequent time points, $i-1$ and $i+1$, respectively. To compensate for cellular movements, we used the optical flow, a vector field that quantifies local changes in image intensity (Raffel et al., 1998) (supplementary material Fig. S1A,B). To calculate the optical flow, we divided image i into 64 by 64 pixel interrogating windows. For each interrogating window, we defined a corresponding search window in image $i+1$ (or $i-1$), centered on the same pixel as the interrogating window and twice as large. We calculated the cross-correlation between interrogating and search windows, and selected the point of maximum cross-correlation as the value of the flow vector at the center of the interrogating window. We shifted each point in the final contour on image i by the closest optical flow vector before projecting the contour into time point $i+1$ (or $i-1$) (Fig. 1D,E). This method was iterated to automatically segment the entire sequence.

3D analysis of cell morphology
To segment cells in 3D, we initialized one snake per cell in one of the planes of the image stack. After energy minimization, snakes were projected onto the adjacent z-planes using optical flow. This process was repeated in all time points of the movie, thus tracking cells in 3D and over time. We applied a Gaussian filter ($\sigma=0.36\,\mu m$) to smoothen the final contours. Reconstructed cells were stretched fivefold along the z-axis for visualization.

3D cell morphology was quantified using a shape factor, defined in analogy to the two-dimensional shape factor (Fernandez-Gonzalez et al., 2009) as:

$$shape(t) = 4\pi h(t)\frac{v(t)}{s(t)^2},\qquad(4)$$

in which $h(t)$, $v(t)$ and $s(t)$ are, respectively, the height, volume and lateral surface area of the reconstructed cells. The shape value is 1 for cylinders and 0 for flat sheets. Prisms with polygonal bases display shape values between 0 and 1.

Quantitative analysis
We established the onset of wound closure as the time at which wound area was at its maximum. The transition from rapid to slow wound repair was determined visually for each wound as the median of the times selected by five independent observers. Measurement error in the segmentation results was quantified as:

$$error(t) = \frac{|reference(t) - target(t)|}{reference(t)} \times 100,\qquad(5)$$

in which $reference(t)$ and $target(t)$ indicate the measurement values obtained with two of the segmentation methods at time point t.

To quantify Abl accumulation at the wound margin, we wounded embryos expressing myosin:mCherry and Abl:GFP. We used MEDUSA to delineate the wound based on the myosin signal. The wound margin mask was a three-pixel-wide ($0.5\,\mu m$) dilation of the wound outline obtained with MEDUSA. We overlaid the wound mask on the Abl:GFP images, and we quantified the mean fluorescence of the pixels under the wound outline. Intensity values were background-subtracted using the image mode as

background value and corrected for photobleaching by dividing by the mean image intensity at each time point. To quantify the increase of fluorescence during wound repair, intensities were normalized to the mean pixel value before wounding within the wounded region. The data were further normalized to the value in the first time point in which the purse string was detected in all movies analyzed (7 min after wounding) to compare across embryos and molecules.

For the analysis of fluorescence dynamics in single cell edges, points delimiting edges were annotated on the MEDUSA segmentation. We used linear interpolation to quantify fluorescence with subpixel resolution at 1000 evenly spaced points along each edge. Intensities were background-subtracted with the mean pixel value outside the embryo and divided by the mean image intensity to normalize for photobleaching. Points were averaged according to their relative position within the edge to normalize for changes in edge length. Vertex intensity was calculated as the average value of the first three points or the last three points in the 1000-point sequence for all edges. Interface intensity was the average of the central 200 points.

To measure actin organization, we imaged wound closure in embryos expressing GFP:moesin. We divided the purse string into quadrants and calculated the actin intensity in each quadrant as the mean pixel value under a three-pixel-wide ($0.6\,\mu m$) dilation of the MEDUSA segmentation. We quantified heterogeneity in the actin distribution as the standard deviation of the quadrant values at each time point. We quantified protrusive activity by creating an annular mask inside the wound with a width of $2.5\,\mu m$ and measuring the fraction of pixels under the mask with values above an intensity threshold (supplementary material Fig. S5). To create the mask, we dilated the wound outline obtained with MEDUSA and selected the pixels that were not part of the original wound delineation and were inside the wound. The intensity threshold was the mean image intensity plus one-and-a-half standard deviations.

Statistical analysis
To compare sample variances, we used the F-test (Glantz, 2002). To compare sample means, we used Student's t-test, applying Holm's correction when three or more groups were considered. Apical volume and surface area changes were evaluated using a paired t-test. To compare time curves, we used the area under each curve as the test statistic. Error bars indicate the standard error of the mean (s.e.m.).

References
Abreu-Blanco, M. T., Verboon, J. M. and Parkhurst, S. M. (2011). Cell wound repair in Drosophila occurs through three distinct phases of membrane and cytoskeletal remodeling. *J. Cell Biol.* **193**, 455-464.
Abreu-Blanco, M. T., Verboon, J. M., Liu, R., Watts, J. J. and Parkhurst, S. M. (2012). Drosophila embryos close epithelial wounds using a combination of cellular protrusions and an actomyosin purse string. *J. Cell Sci.* **125**, 5984-5997.

DEVELOPMENT

Antunes, M., Pereira, T., Cordeiro, J. V., Almeida, L. and Jacinto, A. (2013). Coordinated waves of actomyosin flow and apical cell constriction immediately after wounding. *J. Cell Biol.* **202**, 365-379.

Baum, B. and Perrimon, N. (2001). Spatial control of the actin cytoskeleton in Drosophila epithelial cells. *Nat. Cell Biol.* **3**, 883-890.

Bear, J. E., Svitkina, T. M., Krause, M., Schafer, D. A., Loureiro, J. J., Strasser, G. A., Maly, I. V., Chaga, O. Y., Cooper, J. A., Borisy, G. G. et al. (2002). Antagonism between Ena/VASP proteins and actin filament capping regulates fibroblast motility. *Cell* **109**, 509-521.

Bement, W. M., Forscher, P. and Mooseker, M. S. (1993). A novel cytoskeletal structure involved in purse string wound closure and cell polarity maintenance. *J. Cell Biol.* **121**, 565-578.

Bendix, P. M., Koenderink, G. H., Cuvelier, D., Dogic, Z., Koeleman, B. N., Brieher, W. M., Field, C. M., Mahadevan, L. and Weitz, D. A. (2008). A quantitative analysis of contractility in active cytoskeletal protein networks. *Biophys. J.* **94**, 3126-3136.

Beucher, S. (1992). The watershed transformation applied to image segmentation. *Scanning Microsc Suppl.* **6**, 299-314.

Brock, J., Midwinter, K., Lewis, J. and Martin, P. (1996). Healing of incisional wounds in the embryonic chick wing bud: characterization of the actin purse-string and demonstration of a requirement for Rho activation. *J. Cell Biol.* **135**, 1097-1107.

Bryant, R., Griffiths, P. and Grossman, D. (2003). *Exterior Differential Systems and Euler-Lagrange Partial Differential Equations*. Chicago: University of Chicago Press.

Campos, I., Geiger, J. A., Santos, A. C., Carlos, V. and Jacinto, A. (2010). Genetic screen in Drosophila melanogaster uncovers a novel set of genes required for embryonic epithelial repair. *Genetics* **184**, 129-140.

Chou, T. B. and Perrimon, N. (1996). The autosomal FLP-DFS technique for generating germline mosaics in Drosophila melanogaster. *Genetics* **144**, 1673-1679.

Cohen, L. D. and Cohen, I. (1993). Finite-element methods for active contour models and balloons for 2-D and 3-D images. *IEEE Trans. Pattern Anal. Mach. Intell.* **15**, 1131-1147.

Degen, K. E. and Gourdie, R. G. (2012). Embryonic wound healing: a primer for engineering novel therapies for tissue repair. *Birth Defects Res. C Embryo Today* **96**, 258-270.

Dijkstra, E. W. (1959). A note on two problems in connexion with graphs. *Numerische Math.* **1**, 269-271.

Duda, R., Hart, P. E. and Stork, D. G. (2000). *Pattern Classification* 2nd edn. New York: Wiley-Interscience.

Fernandez-Gonzalez, R. and Zallen, J. A. (2011). Oscillatory behaviors and hierarchical assembly of contractile structures in intercalating cells. *Phys. Biol.* **8**, 045005.

Fernandez-Gonzalez, R. and Zallen, J. A. (2013). Wounded cells drive rapid epidermal repair in the early Drosophila embryo. *Mol. Biol. Cell* **24**, 3227-3237.

Fernandez-Gonzalez, R., Deschamps, T., Idica, A., Malladi, R. and Ortiz de Solorzano, C. (2004). Automatic segmentation of histological structures in mammary gland tissue sections. *J. Biomed. Opt.* **9**, 444-453.

Fernandez-Gonzalez, R., Illa-Bochaca, I., Welm, B. E., Fleisch, M. C., Werb, Z., Ortiz-de-Solorzano, C. and Barcellos-Hoff, M. H. (2009). Mapping mammary gland architecture using multi-scale in situ analysis. *Integr. Biol. (Camb.)* **1**, 80-89.

Fox, D. T. and Peifer, M. (2007). Abelson kinase (Abl) and RhoGEF2 regulate actin organization during cell constriction in Drosophila. *Development* **134**, 567-578.

Gates, J., Mahaffey, J. P., Rogers, S. L., Emerson, M., Rogers, E. M., Sottile, S. L., Van Vactor, D., Gertler, F. B. and Peifer, M. (2007). Enabled plays key roles in embryonic epithelial morphogenesis in Drosophila. *Development* **134**, 2027-2039.

Glantz, S. A. (2002). Primer of Biostatistics. *New York*: McGraw-Hill.

Grevengoed, E. E., Loureiro, J. J., Jesse, T. L. and Peifer, M. (2001). Abelson kinase regulates epithelial morphogenesis in Drosophila. *J. Cell Biol.* **155**, 1185-1198.

Grevengoed, E. E., Fox, D. T., Gates, J. and Peifer, M. (2003). Balancing different types of actin polymerization at distinct sites: roles for Abelson kinase and Enabled. *J. Cell Biol.* **163**, 1267-1279.

Hutson, M. S., Tokutake, Y., Chang, M.-S., Bloor, J. W., Venakides, S., Kiehart, D. P. and Edwards, G. S. (2003). Forces for morphogenesis investigated with laser microsurgery and quantitative modeling. *Science* **300**, 145-149.

Janmey, P. A. (1991). Mechanical properties of cytoskeletal polymers. *Curr. Opin. Cell Biol.* **3**, 4-11.

Janson, L. W., Kolega, J. and Taylor, D. L. (1991). Modulation of contraction by gelation/solation in a reconstituted motile model. *J. Cell Biol.* **114**, 1005-1015.

Juarez, M. T., Patterson, R. A., Sandoval-Guillen, E. and McGinnis, W. (2011). Duox, Flotillin-2, and Src42A are required to activate or delimit the spread of the transcriptional response to epidermal wounds in Drosophila. *PLoS Genet.* **7**, e1002424.

Kass, M., Witkin, A. and Terzopoulos, D. (1988). Snakes: active contour models. *Int. J. Comput. Vision* **1**, 321-331.

Kiehart, D. P., Galbraith, C. G., Edwards, K. A., Rickoll, W. L. and Montague, R. A. (2000). Multiple forces contribute to cell sheet morphogenesis for dorsal closure in Drosophila. *J. Cell Biol.* **149**, 471-490.

Köhler, S., Schaller, V. and Bausch, A. R. (2011). Structure formation in active networks. *Nat. Mater.* **10**, 462-468.

Koleske, A. J., Gifford, A. M., Scott, M. L., Nee, M., Bronson, R. T., Miczek, K. A. and Baltimore, D. (1998). Essential roles for the Abl and Arg tyrosine kinases in neurulation. *Neuron* **21**, 1259-1272.

Lesch, C., Jo, J., Wu, Y., Fish, G. S. and Galko, M. J. (2010). A targeted UAS-RNAi screen in Drosophila larvae identifies wound closure genes regulating distinct cellular processes. *Genetics* **186**, 943-957.

Liu, Z., Tan, L., Cohen, D. M., Yang, M. T., Sniadecki, N. J., Ruiz, S. A., Nelson, C. M. and Chen, C. S. (2010). Mechanical tugging force regulates the size of cell-cell junctions. *Proc. Natl. Acad. Sci. USA* **107**, 9444-9949.

Longaker, M. T., Whitby, D. J., Adzick, N. S., Crombleholme, T. M., Langer, J. C., Duncan, B. W., Bradley, S. M., Stern, R., Ferguson, M. W. J. and Harrison, M. R. (1990). Studies in fetal wound healing VI. Second and early third trimester fetal wounds demonstrate rapid collagen deposition without scar formation. *J. Pediatr. Surg.* **25**, 63-69; discussion 68–69.

Maddox, A. S., Lewellyn, L., Desai, A. and Oegema, K. (2007). Anillin and the septins promote asymmetric ingression of the cytokinetic furrow. *Dev. Cell* **12**, 827-835.

Martin, P. and Lewis, J. (1992). Actin cables and epidermal movement in embryonic wound healing. *Nature* **360**, 179-183.

Martin, A. C., Gelbart, M., Fernandez-Gonzalez, R., Kaschube, M. and Wieschaus, E. F. (2010). Integration of contractile forces during tissue invagination. *J.Cell Biol.* **188**, 735-749.

McCartney, B. M., McEwen, D. G., Grevengoed, E., Maddox, P., Bejsovec, A. and Peifer, M. (2001). Drosophila APC2 and Armadillo participate in tethering mitotic spindles to cortical actin. *Nat. Cell Biol.* **3**, 933-938.

McCluskey, J. and Martin, P. (1995). Analysis of the tissue movements of embryonic wound healing-DiI studies in the limb bud stage mouse embryo. *Dev. Biol.* **170**, 102-114.

Moulding, D. A., Moeendarbary, E., Valon, L., Record, J., Charras, G. T. and Thrasher, A. J. (2012). Excess F-actin mechanically impedes mitosis leading to cytokinesis failure in X-linked neutropenia by exceeding Aurora B kinase error correction capacity. *Blood* **120**, 3803-3811.

Pickering, K., Alves-Silva, J., Goberdhan, D. and Millard, T. H. (2013). Par3/ Bazooka and phosphoinositides regulate actin protrusion formation during Drosophila dorsal closure and wound healing. *Development* **140**, 800-809.

Raffel, M., Willert, C. E. and Kompenhans, J. (1998). *Particle Image Velocimetry: A Practical Guide*. Berlin; New York: Springer.

Reymann, A.-C., Boujemaa-Paterski, R., Martiel, J.-L., Guerin, C., Cao, W., Chin, H. F., De La Cruz, E. M., Thery, M. and Blanchoin, L. (2012). Actin network architecture can determine myosin motor activity. *Science* **336**, 1310-1314.

Rowlatt, U. (1979). Intrauterine wound healing in a 20 week human fetus. *Virchows Arch. A Pathol. Anat. Histol.* **381**, 353-361.

Sonnemann, K. J. and Bement, W. M. (2011). Wound repair: toward understanding and integration of single-cell and multicellular wound responses. *Annu. Rev. Cell Dev. Biol.* **27**, 237-263.

Tamada, M., Farrell, D. L. and Zallen, J. A. (2012). Abl regulates planar polarized junctional dynamics through β-catenin tyrosine phosphorylation. *Dev. Cell* **22**, 309-319.

Whitby, D. J. and Ferguson, M. W. J. (1991). Immunohistochemical localization of growth factors in fetal wound healing. *Dev. Biol.* **147**, 207-215.

Wood, W., Jacinto, A., Grose, R., Woolner, S., Gale, J., Wilson, C. and Martin, P. (2002). Wound healing recapitulates morphogenesis in Drosophila embryos. *Nat. Cell Biol.* **4**, 907-912.

Zandy, N. L. and Pendergast, A. M. (2008). Abl tyrosine kinases modulate cadherin-dependent adhesion upstream and downstream of Rho family GTPases. *Cell Cycle* **7**, 444-448.